Title

Structure-based design of nanobodies that inhibit seeding of Alzheimers patient-extracted tau fibrils.

Journal

Proceedings of the National Academy of Sciences of USA, 120(41)

Authors

Abskharon, Romany
Pan, Hope
Sawaya, Michael
et al.

Publication Date

2023-10-10

DOI

10.1073/pnas.2300258120

Peer reviewed

PNAS RESEARCH ARTICLE | BIOPHYSICS AND COMPUTATIONAL BIOLOGY OPEN ACCESS

Structure-based design of nanobodies that inhibit seeding of Alzheimer's patient–extracted tau fibrils

Romany Abskharon[a,b,c,d,1], Hope Pan[a,b,c,d,1], Michael R. Sawaya[a,b,c,d], Paul M. Seidler[a,b,c,d,2], Eileen J. Olivares[a], Yu Chen[a,e], Kevin A. Murray[a,b,c,d], Jeffrey Zhang[a,b,c,d], Carter Lantz[a,3], Megan Bentzel[a,b,c,d], David R. Boyer[a,b,c,d], Duilio Cascio[a,b,c,d], Binh A. Nguyen[a,b,c,d], Ke Hou[a,b,c,d], Xinyi Cheng[a,b,c,d], Els Pardon[f], Christopher K. Williams[g,h], Alissa L. Nana[i], Harry V. Vinters[g,h], Salvatore Spina[i], Lea T. Grinberg[i,j], William W. Seeley[i,j], Jan Steyaert[f], Charles G. Glabe[k], Rachel R. Ogorzalek Loo[a,b,d], Joseph A. Loo[a,b,d], and David S. Eisenberg[a,b,c,d,4]

Edited by Thomas Südhof, Stanford University, Stanford, CA; received January 16, 2023; accepted August 21, 2023

Despite much effort, antibody therapies for Alzheimer's disease (AD) have shown limited efficacy. Challenges to the rational design of effective antibodies include the difficulty of achieving specific affinity to critical targets, poor expression, and antibody aggregation caused by buried charges and unstructured loops. To overcome these challenges, we grafted previously determined sequences of fibril-capping amyloid inhibitors onto a camel heavy chain antibody scaffold. These sequences were designed to cap fibrils of tau, known to form the neurofibrillary tangles of AD, thereby preventing fibril elongation. The nanobodies grafted with capping inhibitors blocked tau aggregation in biosensor cells seeded with postmortem brain extracts from AD and progressive supranuclear palsy (PSP) patients. The tau capping nanobody inhibitors also blocked seeding by recombinant tau oligomers. Another challenge to the design of effective antibodies is their poor blood–brain barrier (BBB) penetration. In this study, we also designed a bispecific nanobody composed of a nanobody that targets a receptor on the BBB and a tau capping nanobody inhibitor, conjoined by a flexible linker. We provide evidence that the bispecific nanobody improved BBB penetration over the tau capping inhibitor alone after intravenous administration in mice. Our results suggest that the design of synthetic antibodies that target sequences that drive protein aggregation may be a promising approach to inhibit the prion-like seeding of tau and other proteins involved in AD and related proteinopathies.

nanobody | amyloid | tau | prion-like spreading | synthetic antibody

Significance

Alzheimer's disease (AD) is associated with aggregation of the protein tau in the brain. Antibodies that bind tau and halt its aggregation are one approach to slowing the progression of AD; however, traditional animal-produced antibodies are often limited by weak target binding, low production, and low brain delivery. We propose a method for designing antibodies in which we graft tau-specific sequences into a camelid antibody fragment or "nanobody". Our engineered nanobodies are easily produced and block the propagation of tau aggregation in test tube experiments. Next, by linking our best tau-targeting nanobody behind a brain-targeting nanobody, we created a double nanobody designed to enter the brain. Our results demonstrate an alternative approach to engineering antibodies to target tau aggregation.

Alzheimer's disease (AD) is the most common neurodegenerative condition, accounting for dementia in dozens of millions of people worldwide (1–3). Tau pathology appears in AD when the protein tau transitions into amyloid fibrils, which can spread from cell to cell in a prion-like manner (4, 5). Many amyloid proteins, including tau, Aβ, and α-synuclein aggregate into "cross-β" filaments featuring β-sheets that run the length of the fibrils, stabilized by steric zippers. Steric zippers are paired β-sheets mated by tightly interdigitated side chains (2, 3, 6). Most zipper interfaces exclude water molecules, contributing to filament stability (7).

We previously determined high-resolution structures of the SVQIVY, VQIVYK, and VQIINK amyloid-driving segments of tau using microelectron and X-ray crystallography (8–12). The hexapeptide segments VQIVYK and VQIINK are believed to drive tau aggregation and seeding (8, 13). Our structures of SVQIVY, VQIINK, and VQIVYK reveal aggregation interfaces that we have used to design fibril-capping peptide inhibitors that block tau aggregation and seeding (8, 9, 12).

Recently, cryoelectron microscopy has provided structural views of tau polymorphs isolated from patients with tauopathies including AD, chronic traumatic encephalopathy, Pick's disease, and corticobasal degeneration (14–18). The structures of paired helical filaments (PHF) and straight filaments (SF) extracted from patients with AD reveal tau molecules in cross-β folds, which are stabilized by steric zippers (7, 14). All show the VQIVYK segment in the core of fibrillar tau. These structural studies of fibrils extracted from postmortem tauopathy brains support the disease relevance of the SVQIVY, VQIINK, and VQIVYK tau segments as targets for designed inhibitors.

Immunotherapeutic approaches show promise of being effective in treating AD at early stages (19, 20). Several studies have recently demonstrated that tau-targeted immunization is a promising therapeutic approach to slow tau accumulation and PHF pathology in transgenic mouse models of tauopathies (21–24). For example, dual administration of antibodies PHF1, which recognizes S396- and S404-phosphorylated tau, and MC1, which recognizes tau in a pathological conformation, reduced tau pathology and neurodegeneration in two

Competing interest statement: D.S.E. is SAB chair and an equity holder of ADRx, Inc.

This article is a PNAS Direct Submission.

[1]R.A. and H.P. contributed equally to this work.

[2]Present Address: Department of Pharmacology and Pharmaceutical Sciences, University of Southern California School of Pharmacy, Los Angeles, CA 90089.

[3]Present Address: Department of Chemistry, Texas A&M University, College Station, TX 77843.

[4]To whom correspondence may be addressed. Email: david@mbi.ucla.edu.

This article contains supporting information online at https://www.pnas.org/lookup/suppl/doi:10.1073/pnas.2300258120/-/DCSupplemental.

Published October 6, 2023.

different mouse models (25). These promising preclinical studies have led to clinical trials of many anti-tau antibodies (26).

Structure-based design offers advantages over classical methods for generation of de novo antibodies. Classical immunization strategies are limited in practice by the ability to produce an effective antigen that elicits, from an inoculated animal, an antibody structure specific for the desired epitope. Classical strategies often resort to antigens with low immunogenicity which redirects the generation of antibodies away from important epitopes (27). In contrast, structure-based design takes advantage of knowledge of the epitope structure to customize antibody specificity and affinity and can be a quicker route to success provided it is possible to overcome potential pitfalls of aggregation propensity, expression difficulties in prokaryotic cells, and high cost of protein production.

In choosing a system for structure-based antibody design, camelid heavy chain-only antibodies (VHH), or nanobodies, are an alternative to the traditional immunoglobulin antibody that can overcome the aforementioned pitfalls. Owing to their small size, high stability, and robust structure, they can access hidden epitopes with excellent tissue penetration in vivo, are amenable to protein engineering, and can be expressed in a variety of microorganisms (28, 29). In early 2019, the FDA approved the first nanobody for acquired thrombotic thrombocytopenic purpura, a rare blood disorder characterized by blood clotting in small blood vessels (30). FDA approval of a nanobody therapeutic sets precedence that encourages the development of nanobodies to treat other pathologies, like neurodegenerative disorders.

Immunotherapies to treat neurological disorders, whether identified by classical or structure-based strategies, face the challenge of penetrating the blood–brain barrier (BBB) (31). Immunotherapies that cannot passively cross the BBB can be delivered using receptor-mediated transcytosis (RMT), a pathway for transport of macromolecules across the BBB (32). A promising receptor for RMT is insulin-like growth factor-1 receptor (IGF1R) which is expressed on brain endothelial cells. In previous studies, nanobodies have been raised against IGF1R by immunizing a llama with an IGF1R polypeptide (33, 34). The nanobodies were demonstrated to cross the BBB in in vitro transwell models and in animal models (34, 35). Conjugation of an IGF1R-binding nanobody to immunotherapies for AD could potentially surmount the obstacle of their limited BBB penetrability.

Here, we build on an earlier antibody design strategy in which small amyloidogenic motifs of Aβ (6 to 10 residues) were grafted into the variable region to create antibodies for detection and inhibition of Aβ fibrils and oligomers (36). In our study, we graft capping peptide inhibitors of tau into the variable region of a heavy chain camel antibody. We designed two generations of synthetic camel antibodies that halt prion-like seeding. In addition, we designed a bispecific nanobody that both serves as a capping inhibitor of tau and targets IGFR1 for delivery to the brain via RMT. Our work evaluates whether therapeutic nanobodies may be constructed by incorporating inhibitors of steric-zipper sequences that drive protein aggregation and seeding.

Results

Design of First-Generation Nanobody Inhibitors of tau Aggregation. Here, we extend previous work on peptide-based inhibitors, designed to bind tau at the tips of amyloid fibrils and sterically interfere with fibril growth. These inhibitors were designed to bind to the amyloid-driving sequences VQIINK and VQIVYK of tau, and they are termed W3 and WIW, respectively (8, 11, 12). In addition to these previous capping peptide designs, we include an additional inhibitor design, VDW, a derivative of WIW that is extended by six residues at its C-terminal end to provide additional H-bonding with the complementary sequence downstream of VQIVYK. VDW binding is bolstered by a charge reversal at its C terminus to promote ion pairing with tau Lys317, and VDW bears a Trp substitution at position 11, which would overlap with extraneous density on the surface of the AD-tau fibril reported to derive from ubiquitin (15). In short, the VDW sequence, SVWIWYEPVDWSE, is designed to bind the tau segment 305-SVQIVYKPVDLSK-317.

To design antibodies that target tau aggregation, we grafted the three individual capping inhibitory sequences VDW, W3, and WIW into the complementarity determining region 3 (CDR3) of a previously reported nanobody scaffold (37) (PDB entry ID: 6HEQ) (Fig. 1*A* and *SI Appendix*, Table S1). WIW and VDW nanobody fusions were designed to disrupt the VQIVYK steric zipper, while the W3 nanobody inhibitor was designed to target the VQIINK steric zipper. We call these VDW, W3, and WIW nanobodies the first generation of tau nanobody inhibitors.

To increase the conformational flexibility of the grafted nanobody inhibitor sequence, we inserted $(glycine)_3$ at both N and C termini of the grafted insert of the CDR3 loop. We expressed the designed nanobodies with a pelB leader sequence for expression in the bacterial periplasm with yields in the milligram range with >95% purity (Fig. 1*B* and *SI Appendix*, Fig. S1 *A–C*). Purification by size-exclusion chromatography (SEC) of the designed nanobody reveals a prominent peak of VDW, W3, and WIW nanobodies (*SI Appendix*, Fig. S1 *A–C*).

Assessment of Nanobody Binding to tau. We employed dot blot analysis to determine whether our nanobody is specific for binding recombinant tau-K18 monomers, prefibrillar oligomers, or fibrils (Fig. 1*C*). Tau-K18 is a truncated tau construct containing the four microtubule-binding domains R1–R4 (residues 244 to 372) (38). Dot blots confirmed the nanobody bearing the VDW inhibitor sequence recognizes tau-K18 in both the monomer and fibril states, suggesting that the binding epitope of both monomer and fibril is accessible to the designed nanobody.

Crystal Structure of the WIW Nanobody Inhibitor and Docking Simulations. The X-ray crystal structure of the WIW nanobody was determined to high (1.4 Å) resolution (Fig. 1*D* and *SI Appendix*, Table S2). The WIW nanobody crystallized with one monomer in the asymmetric unit in space group I4 and with unit cell dimensions a = 78.29 b = 78.29 and c = 38.22 Å. The WIW nanobody shows well-resolved electron density and displays an immunoglobulin fold with a β-sandwich formed by two antiparallel β-sheets. The WIW nanobody possesses three complementarity-determining regions or CDR loops (CDR1, CDR2, and CDR3) as shown in Fig. 1*D*. When grafted into the CDR3 loop, the WIW inhibitor adopts a beta-strand conformation that is compatible with steric zipper capping (Fig. 1*D*). The crystal structure shows that the designed nanobody structure agrees with the design.

We docked the determined crystal structure of the WIW nanobody to the previously published PHF structure (Fig. 1 *E* and *F*). The CDR3 loop in the nanobody structure adopts a beta-strand secondary structure compatible with binding the steric zipper at the tip of the PHF fibril.

We pursued structural studies to investigate whether the designed WIW-tau interface (approximated in Fig. 1 *E* and *F*) is indeed responsible for the observed inhibition of tau fibril growth by WIW (Fig. 1 *G* and *H*). Our first strategy was to cocrystallize

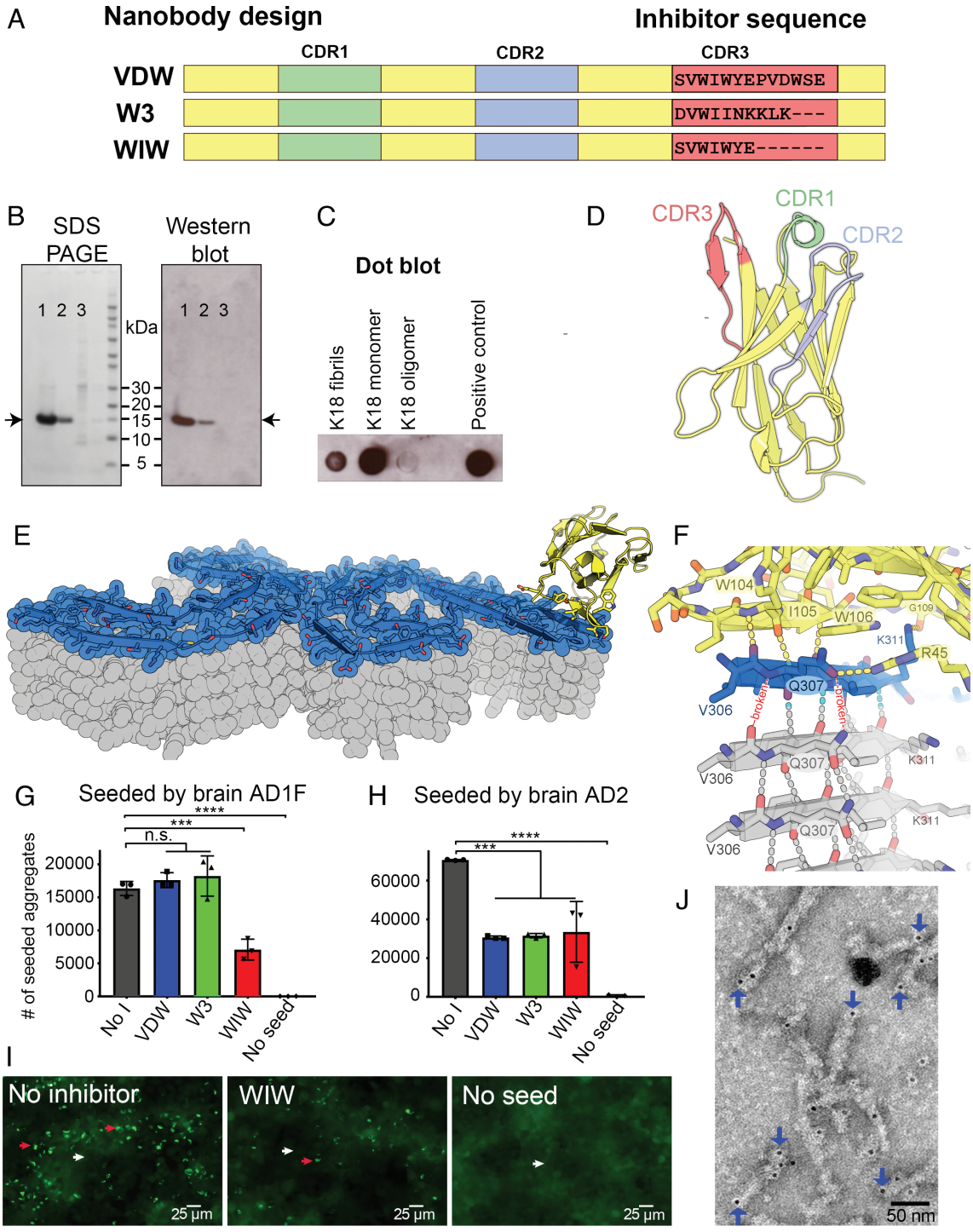

Fig. 1. Design and testing of first-generation nanobody inhibitors of tau seeding. (*A*) Schematic representation of nanobody designs. The tau inhibitor sequences are grafted into the CDR3 of heavy chain of VDW, W3, and WIW nanobodies. (*B*) SDS/PAGE and western blot analysis of VDW nanobody purification using anti-His tag antibody, lanes 1 and 2 = nanobody elution fractions, lane 3 = flow-through. The SDS/PAGE gel was stained with Coomassie blue. (*C*) Dot blot showing immunoreactivity of VDW nanobody toward fibrils and monomer of tau-K18. The positive control protein is unrelated to tau and has a His tag. (*D*) X-ray crystal structure of the WIW nanobody inhibitor showing its CDRs. CDR1 in green, CDR2 in blue, and CDR3 in red. (*E*) Model of the WIW nanobody inhibitor (yellow) capping the end of PHF filament with the top layer shown in blue. (*F*) Detailed model of the hydrogen-bonded interaction (yellow dotted lines) of the designed inhibitor and PHF fibrils. The side chain interaction is shown in yellow dots, whereas the broken hydrogen bonds are shown in red dots. (*G* and *H*) Quantification of the effects of VDW, W3, and WIW nanobodies on inhibition of seeding by brain extracts from AD brain tissues (AD1 F, frontal lobe and AD2), measured in HEK293 biosensor cells expressing YFP-tagged tau-K18. The inhibitor concentration of all nanobodies was 10 μM on the biosensor cells. The experiment was performed in technical triplicate. Statistical analysis was performed using one-way ANOVA followed by a Tukey's multiple comparison test (ns, $P > 0.05$; *$P \le 0.05$; **$P \le 0.01$; ***$P \le 0.001$; ****$P \le 0.0001$) in GraphPad Prism. (*I*) Representative images of seeding and inhibition in HEK293 biosensor cells expressing YFP-tagged tau-K18. Cells seeded with brain extracts from AD Donor 2 (AD2) without pretreatment with nanobodies (*Left*), and following overnight incubation with WIW nanobody (as indicated). Representative cells that contain aggregates are marked by red arrows and cells without by white arrows. (*J*) Representative EM of immuno-gold labeling with antibodies of VDW nanobody, and tau-k18 fibrils. Fibril binding at the tip is marked by blue arrows.

the WIW nanobody with tau epitope 306-VQIVYK-311; however, only crystals of the WIW nanobody resulted (Fig. 1*D*). So, we turned our efforts toward computationally docking the nanobody WIW crystal structure (8fq7) on the tau PHF structure (7nrv). The results of our unbiased docking study reproduced some features of our design and suggested strategies for improvement. Three of the 29 docking models produced by ClusPro (39) featured interfaces involving the intended nanobody WIW and tau VQIVYK segments. However, the two segments exhibited antiparallel rather than parallel alignment in two of the models and out-of-register rather than in-register in the third model. These deviations from our design may result in part from the limitations arising from the rigid body docking approximation. The deviations could also be incurred by the docking program's drive to supplement the relatively small interface in our design with additional contacts involving regions outside CDR3. Last, we note that further engineering of the linker between inhibitor insert and scaffold might improve the interface with tau. E108 in our crystal structure of the WIW nanobody (*SI Appendix*, Fig. S1*E*) was not oriented to form a salt bridge with tau residue K311 as designed (*SI Appendix*, Fig. S1*D*), presumably constrained by the linker connecting it to the scaffold.

Designed Nanobodies Block Seeding by tau Fibrils and Oligomers in HEK293 Biosensor Cells. We evaluated the efficacies of the nanobody designs to inhibit seeded aggregation in HEK293 cell lines stably expressing tau-K18 P301S-eYFP (yellow fluorescent protein), referred to as "tau biosensor cells". Specifically, we quantified and analyzed the number of puncta (tau-K18 aggregates) seeded by postmortem brain tissue extracts from donors with AD (*SI Appendix*, Table S3) using Image J software. We tested all three nanobodies at a concentration of 10 μM. As shown in Fig. 1 *G–I*, seeding by brain tissue extracts from donor 1 (AD1) and donor 2 (AD2) was inhibited by the WIW capping nanobody inhibitor ($P < 0.0005$). The VDW and W3 nanobodies failed to block tau seeding by brain extracts from AD1, but inhibited tau seeding by brain extracts from AD2, suggesting lower potency of the VDW and W3 nanobody designs. Our evidence suggests that inhibition exhibited by WIW is caused by the designed insert and not the scaffold. If the scaffold had been responsible for the inhibition exhibited by nanobody WIW (Fig. 1*G*), then VDW and W3 would have exhibited the same level of inhibition as WIW since all three share the same scaffold.

To validate the binding of the designed inhibitor to the fibril tips, we used Immuno-EM labeling in conjunction with electron microscopy. As shown in Fig. 1*J*, the VDW nanobody binds to tau-k18 fibril tips, showing the binding to the fibrils agrees with the design. However, the VDW nanobody also binds to the sides of the fibrils. These binding sites along the sides of the fibrils may correspond to points of secondary nucleation of monomeric tau along the primary fibril that may also have an exposed epitope (40). Alternatively, the binding sites of the fibrils may be points of nonspecific binding.

Next, we tested the efficacy of our capping nanobody inhibitors on aggregation seeded by recombinant tau-K18 oligomers prepared by ionic liquid 15 (IL15) as described previously (38). We used tau oligomers because they are hypothesized to promote neurotoxicity (41, 42). An EM image of recombinant tau-K18 oligomers (*SI Appendix*, Fig. S1*F*) reveals a mixture of 10 to 20 nm spherical oligomers has the capability to spread from cell to cell in a prion-like fashion (*SI Appendix*, Fig. S1 *G* and *H*). Seeding by tau-K18 oligomers was reduced by all nanobody designs. Notably, the WIW nanobody inhibited aggregation seeded by both PHFs and oligomers (*SI Appendix*, Fig. S1 *G* and *H*).

Design and Testing of Second-Generation Nanobody Inhibitors of tau Seeding. It has been reported that nanobodies with isoelectric points (pI) above 9.4 spontaneously penetrate cells, making them suitable for targeting intracellular proteins (43). As a result, we sought other nanobody scaffolds with extremely basic pIs, assuming they are more suitable for targeting intracellular tau protein than scaffolds with acidic pIs. To design the second generation of nanobody inhibitors, we selected a previously described nanobody scaffold with pI = 9.8, termed "scaffold 2" (44). We replaced its CDR3 with select inhibitory sequences; one construct bearing the WIW inhibitor sequence and another bearing the native tau SV sequence (Fig. 2*A* and *SI Appendix*, Table S4). We reasoned that the native tau segment could home the nanobody inhibitor to tau and that the fused nanobody itself could sterically prevent binding of additional tau monomers to the tips of fibrils. The WIW and SV second-generation nanobodies were expressed in bacteria (*SI Appendix*, Fig. S2 *A* and *B*). To validate the efficacy of this second generation of nanobody designs for inhibiting tau aggregation, we tested the prion-like seeding of four AD patient brain extracts (*SI Appendix*, Table S3) in the presence or absence of the designed nanobodies using tau biosensor cells. We found that treating the AD brain extracts with the WIW or SV second-generation nanobody strongly reduced the seeding by all four AD samples (*SI Appendix*, Fig. S2 *C–J*).

We further explored our second generation of nanobody design by grafting another four capping inhibitory sequences of W3, M4, R9, and QIINK onto the CDR3 of a nanobody scaffold 2 (Fig. 2*A* and *SI Appendix*, Table S4). W3, M4, and R9 second-generation nanobody inhibitors were designed to disrupt the A, B, and C interfaces in the VQIINK steric zipper, respectively (12). The QIINK nanobody contains a graft of the wild-type tau sequence into the CDR3 of scaffold 2 (Fig. 2*A* and *SI Appendix*, Table S4). Purification of the W3, M4, R9, and QIINK nanobodies produced high-purity products after Ni-NTA column purification but with lower yield than in the scaffold 1 expression (*SI Appendix*, Fig. S3*A*). Therefore, we did not perform SEC after Ni-NTA purification. Western blot analysis of the capping nanobody inhibitors reveals a 15-kDa band consistent with the size analyzed by SDS PAGE (*SI Appendix*, Fig. S3*B*).

We tested the efficacy of our nanobody panel to inhibit seeding by eight AD brain extracts in biosensor cells (*SI Appendix*, Table S3). EM examination of a partially purified brain extract from AD donor 3 (AD3) showed an abundance of PHFs with helical morphology (Fig. 2*B*). The concentration of tau in AD brain extracts was estimated to be 1.5 to 2 μM. To ensure that our capping nanobody inhibitors are specific and target the aggregation-prone segments, we used a noncognate nanobody to serve as a negative control (44). The noncognate nanobody has the same scaffold and high pI as the designed second-generation nanobodies, including CDR1 and CDR2, but a different CDR3 (*SI Appendix*, Table S4). We initially tested all nanobodies at a concentration of 10 μM. All synthetic nanobodies strongly reduced seeding by AD3, AD4, and AD5 patient brain samples (Fig. 2 *C–E* and *SI Appendix*, Fig. S3 *C–E*). We observed some nonspecific inhibition by the noncognate nanobody toward AD3, but the inhibition from all designed nanobodies was significantly greater ($P < 0.0001$) than that of the noncognate.

In addition, all synthetic nanobodies strongly reduced seeding by AD6, AD7, AD8, AD9, and AD10 patient brain samples (*SI Appendix*, Fig. S4). Interestingly, some of the grafted nanobody designs exhibited variation toward seeding inhibition. WIW was the most potent inhibitor of seeding by AD3, AD4, and AD5 brain extracts but was less effective on AD7 and AD8 brain

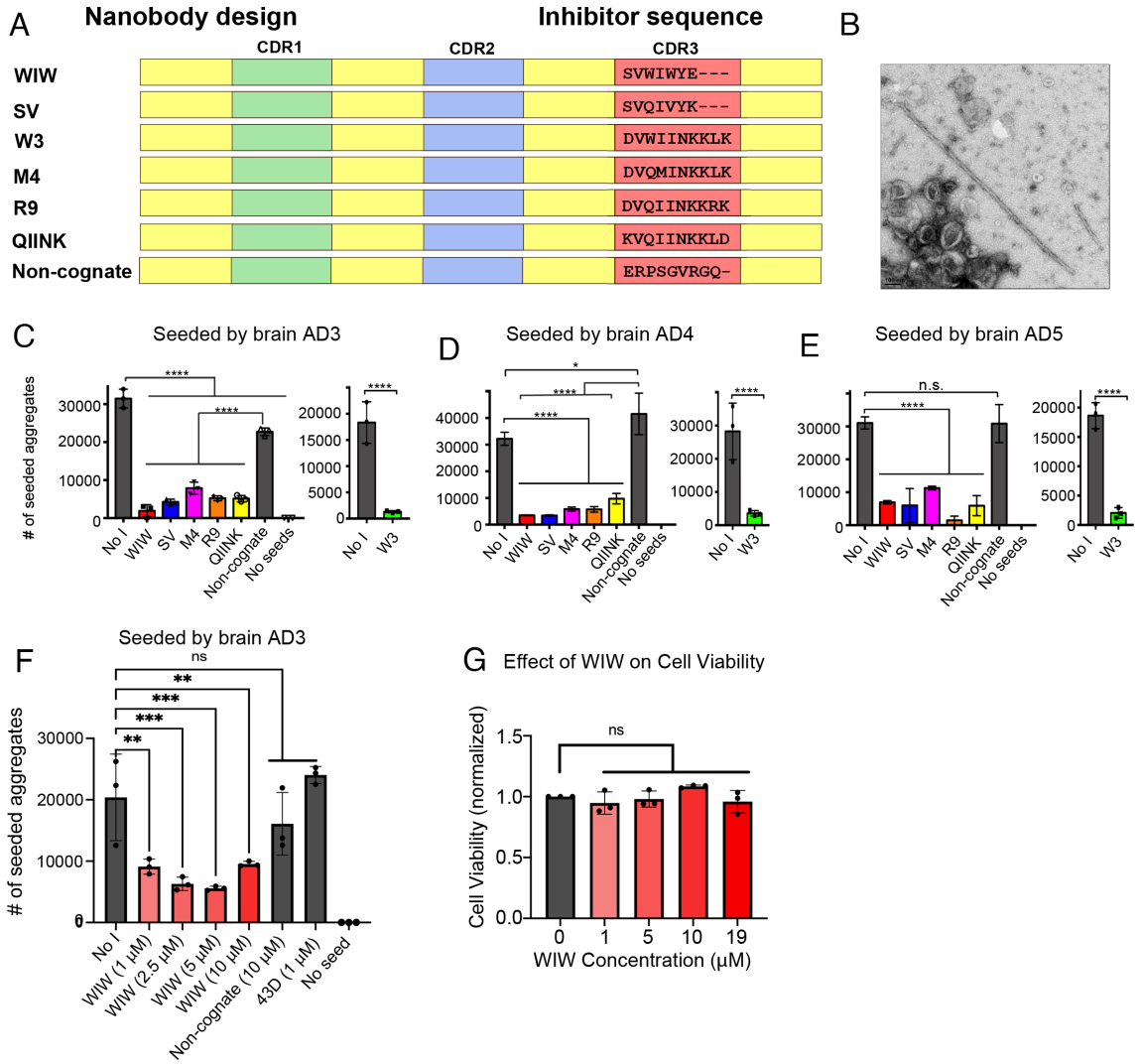

Fig. 2. Design and testing of second-generation capping nanobodies that inhibit the seeding of tau aggregation by extracts from autopsied brains of AD patients. (*A*) Schematic representation of nanobody designs, showing the tau inhibitor sequences grafted into the CDR3 of heavy chain of the WIW, SV, W3, M4, R9, and QIINK nanobodies. (*B*) EM of fibrils from AD patient brain extract (AD3). (Scale bar 100 nm). Brain-extracted fibrils show two twisted protofilaments. (*C*–*E*) Quantification of the effects of WIW, SV, W3, M4, R9, QIINK, and noncognate nanobodies on inhibition of seeding by AD patient brain extracts. The inhibitor concentration of all nanobodies was 10 μM on the biosensor cells. The experiment was performed in technical triplicate. Statistical analysis was performed using one-way ANOVA followed by a Tukey's multiple comparison test (ns, $P > 0.05$; *$P \le 0.05$; **$P \le 0.01$; ***$P \le 0.001$; ****$P \le 0.0001$) in GraphPad Prism. (*C*) AD3. (*D*) AD4. (*E*) AD5. "No I" indicates no inhibitor. (*F*) Representative second-generation nanobody WIW inhibits seeding by brain extract AD3 at doses ranging from 1 to 10 μM. The experiment was performed in technical triplicate. Statistical analysis was performed using one-way ANOVA followed by a Tukey's multiple comparison test (ns, $P > 0.05$; *$P \le 0.05$; **$P \le 0.01$; ***$P \le 0.001$; ****$P \le 0.0001$) in GraphPad Prism. (*G*) Representative second-generation nanobody WIW demonstrates no toxicity toward Neuro 2A cells. The experiment was performed in technical triplicate. Statistical analysis was performed using one-way ANOVA followed by a Tukey's multiple comparison test (ns, $P > 0.05$; *$P \le 0.05$; **$P \le 0.01$; ***$P \le 0.001$; ****$P \le 0.0001$) in GraphPad Prism.

extracts (Fig. 2 *C*–*E* and *SI Appendix*, Fig. S4). SV and M4 nanobodies were more effective inhibitors of AD7 and AD8 than WIW (Fig. 2 *C*–*E* and *SI Appendix*, Fig. S4). The noncognate nanobody showed no effect on seeding by AD6, AD7, AD9, and AD10. We observed nonspecific inhibition by the noncognate nanobody toward AD8.

Next, we tested whether representative second-generation nanobody WIW inhibits seeding by AD3 brain extract at various doses. WIW inhibits seeding by AD3 brain extract in a dose-dependent manner from 1 to 5 μM, and at 10 μM, there is a plateau in WIW's inhibitory effect (Fig. 2*F*). We again used a noncognate nanobody to serve as a negative control which showed no effect on seeding. In addition, we wanted to ensure that our capping nanobody does not simply bind and sequester tau monomer instead of blocking fibril growth. We included a monoclonal antibody that binds residues 6 to 18 of tau, called 43D, and found that it does not reduce seeding by AD3 brain extract. Because 43D can bind tau monomer with high affinity but still does not reduce seeding, we can assume that sequestering tau monomer is not sufficient for nanobody function.

Finally, to assess the toxicity of our nanobodies, we performed a dose-dependent cell viability assay with representative second-generation nanobody WIW and found that WIW has no measurable toxicity toward Neuro 2A cells (Fig. 2*G*).

Nanobody Inhibitors Block Seeding by tau-K18 Oligomers. Next, we sought to determine whether our designed nanobody inhibitors could block seeding by tau oligomers. Both fibrils and oligomers can seed aggregation and thus may be targeted with our designed nanobodies. To determine whether tau oligomers can be targeted by nanobody inhibitors, we prepared tau-K18 oligomers with IL15 as previously described (Fig. 3 *A*–*C*) (38). The formation

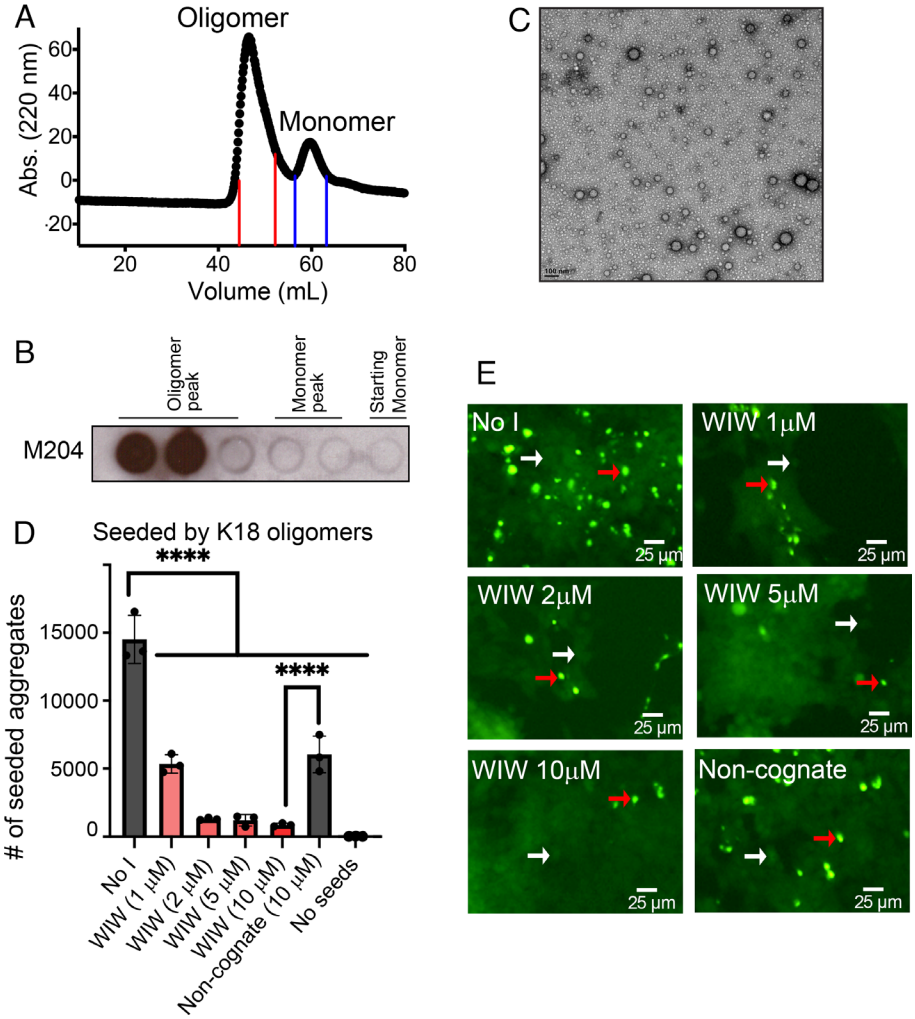

Fig. 3. Inhibition of seeding by tau-K18 oligomers using the second generation of WIW and SV capping nanobodies. (*A*) Purification of tau-K18 oligomers after SEC using an S75 10/300 column as previously described (38). Fractions marked between the solid lines were pooled for use. (*B*) Dot blot of tau-K18 oligomer (left set of three) and monomer (middle set of two) fractions eluted from SEC column and starting tau-K18 monomer used to form oligomers (right sample). M204 is anti-oligomer monoclonal antibody that binds tau-K18 oligomer but not monomer. (*C*) Electron micrographs of tau-K18 oligomers show spherical particles with a diameter of 10 to 20 nm. (Scale bar 100 nm.) (*D*) Representative second-generation nanobody WIW inhibits seeding by tau K18 oligomers at doses ranging from 1 to 10 μM. The experiment was performed in technical triplicate. Statistical analysis was performed using one-way ANOVA followed by a Tukey's multiple comparison test (ns, $P > 0.05$; *$P \le 0.05$; **$P \le 0.01$; ***$P \le 0.001$; ****$P \le 0.0001$) in GraphPad Prism. (*E*) Representative images of seeding and inhibition by WIW and SV nanobodies. Representative cells containing aggregates are marked by red arrows and cells without by white arrows.

of tau-K18 oligomers was confirmed using the M204 antibody, which is specific for tau oligomers but not monomers (Fig. 3*B*) (38). We initially tested all nanobodies at a concentration of 10 μM. We observed that seeded aggregation by tau-K18 oligomers was strongly inhibited in the presence of the second-generation WIW and SV nanobodies in tau biosensor cells (*SI Appendix*, Fig. S2 *K* and *L*).

Next, we tested whether representative second-generation nanobody WIW inhibits seeding by tau-K18 oligomers at various doses. WIW inhibits seeding by oligomers in a dose-dependent manner from 1 to 10 μM (Fig. 3 *D* and *E*). We again used a noncognate nanobody to serve as a negative control. We observed nonspecific inhibition by the noncognate nanobody, but the inhibition from WIW at the same concentration was significantly greater than that of the noncognate ($P < 0.0001$).

Synthetic Nanobodies Block Seeding by Purified Fibrils from Human AD and PSP Brain Tissue. To validate the efficacy of our nanobody designs for targeting disease-relevant amyloid fibrils, we extracted and purified tau fibrils from the brain tissue of AD3 using a water extraction protocol as previously described (45). We used immuno-EM combined with electron microscopy to verify that the purified AD fibrils were composed of tau (Fig. 4*A*). Then, we tested the efficacy of the nanobody capping inhibitors in preventing seeding by the purified tau fibrils. As shown in Fig. 4 *B* and *C*, the designed nanobody inhibitors block seeding by purified tau fibrils, while the noncognate nanobody shows no effect on seeding inhibition. Our nanobody designs successfully inhibit seeding of both crude brain extract and purified tau fibrils from AD patients, revealing the potential relevance of our nanobody-based designs to AD.

In addition to AD brain extracts, we expanded our evaluation of designed nanobody capping inhibitors to include postmortem brain extracts from donors diagnosed with other tauopathies. We tested the inhibitory power of our synthetic nanobodies on crude brain extracts from two donors with PSP. Electron micrographs of brain extract from PSP donor 1 confirmed that the extract contained fibrils with a twisted filament morphology (*SI Appendix*, Fig. S5 *A* and *B*).

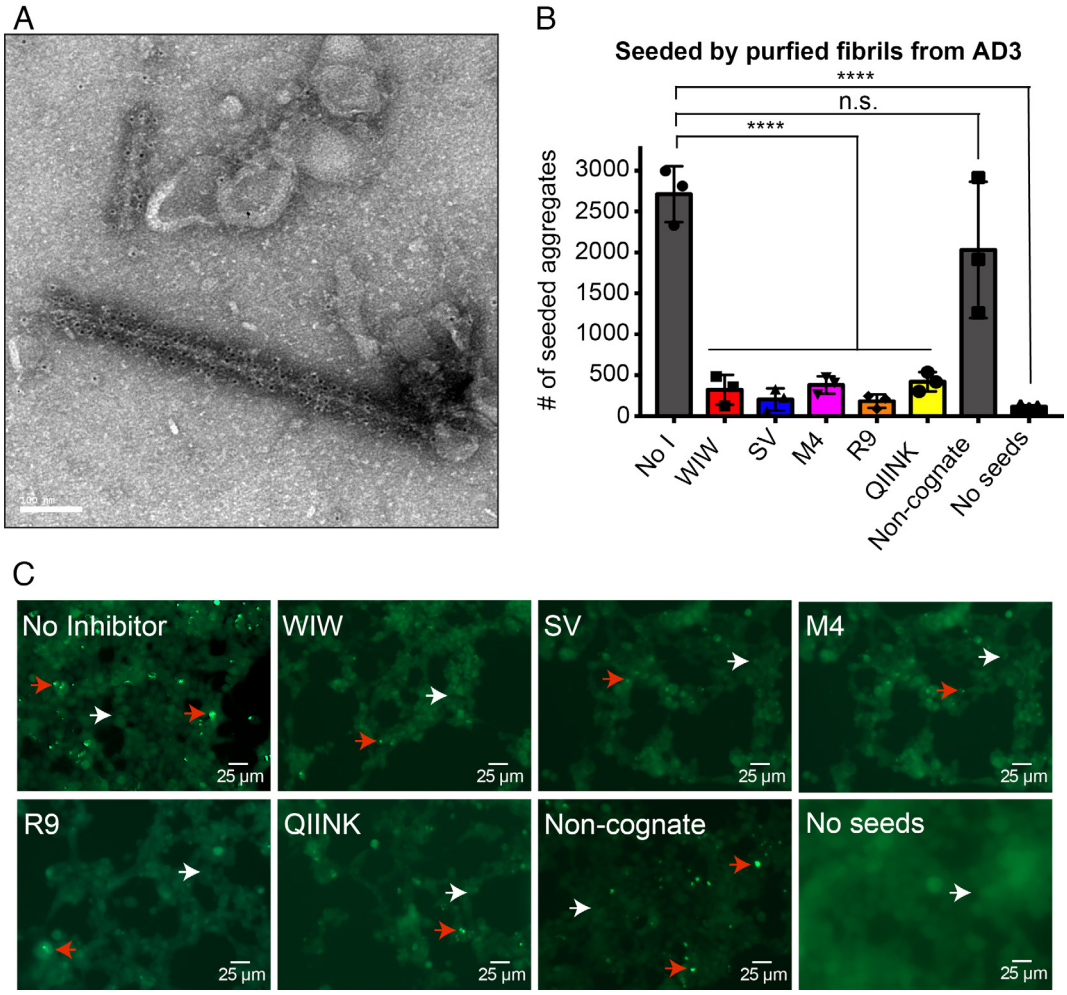

Fig. 4. Designed capping nanobodies inhibit the seeding of purified tau fibrils from a human brain donor with AD pathology. (*A*) Electron micrograph of purified fibrils from brain donor AD3 immunogold labeled by an anti-tau antibody. (*B*) Quantification of the inhibitory effect of WIW, SV, M4, R9, QIINK, and noncognate nanobodies on inhibition of seeding by purified AD brain fibrils (AD3). The inhibitor concentration of all nanobodies was 10 µM on the biosensor cells. The experiment was performed in technical triplicate. Statistical analysis was performed using one-way ANOVA followed by a Tukey's multiple comparison test (ns, $P > 0.05$; *$P \le 0.05$; **$P \le 0.01$; ***$P \le 0.001$; ****$P \le 0.0001$) in GraphPad Prism. (*C*) Representative images of seeding and inhibition of AD3 fibrils in HEK293 biosensor cells expressing YFP-tagged tau-K18. Representative cells containing aggregates are marked by red arrows and cells without by white arrows. The abbreviation of no inhibitor is "No I".

As shown in *SI Appendix*, Fig. S5 *C–E*, all synthetic nanobodies blocked seeding by both PSP brain extracts. The noncognate nanobody showed no effect on seeding by either PSP extract.

Designing a Bispecific WIW Nanobody that Crosses the BBB. To facilitate the delivery of tau inhibitors to wild-type mouse brains, we designed a bispecific nanobody composed of IR5, a nanobody that targets the type 1 IGF1R and has been shown to cross the BBB, and the WIW nanobody inhibitor, conjoined by a flexible linker (Fig. 5*A*) (46). The SEC peak of the bispecific nanobody reveals a ~30-kDa band consistent with the size analyzed by SDS PAGE (Fig. 5 *B* and *C*). To validate brain penetration, the bispecific nanobody was administered by tail vein injection at a dose of 20 mg/kg to C57BL/6J mice (n = 3). As a comparison, the second-generation WIW nanobody was administered at an equimolar dose of 10 mg/kg to C57BL/6J mice (n = 3). Thirty min after dosing, the mice were killed by cardiac perfusion, and brain samples were collected.

Quantitative liquid chromatography–tandem mass spectrometry (LC–MS/MS) determined the bispecific WIW nanobody concentrations in three mouse brains to be 4.3 to 8.1 µg per g, while concentrations of second-generation WIW in three mice were measured as 0 µg per g (Fig. 5*D*). Concentrations were assessed by comparing signal levels in the samples to those derived from the nanobody-spiked brain tissues of nanobody-naive mice (*SI Appendix*, Figs. S6–S8). The brain sample extraction protocol has been described previously (47).

Discussion

Much effort has been applied to design antibodies to target specific, disease-relevant epitopes (27, 48). Limiting the success of this approach are the challenges of predicting CDR loop sequences that confer specific binding to their antigens as well as adequate antibody expression and stability (49, 50). To produce a panel of antibodies capable of halting pathogenic tau aggregation and prion-like seeding, we employed a grafting approach, inserting previously developed inhibitory peptides into CDR3 of a previously reported nanobody scaffold. These inhibitors were designed to target steric zipper interfaces (aggregation-driving structural motifs) that we identified in tau fibrils (8–12). We chose nanobodies as vehicles for enhancing inhibitor delivery and efficacy because 1) nanobodies can be easily engineered and expressed in both eukaryotic and prokaryotic systems with robust protein

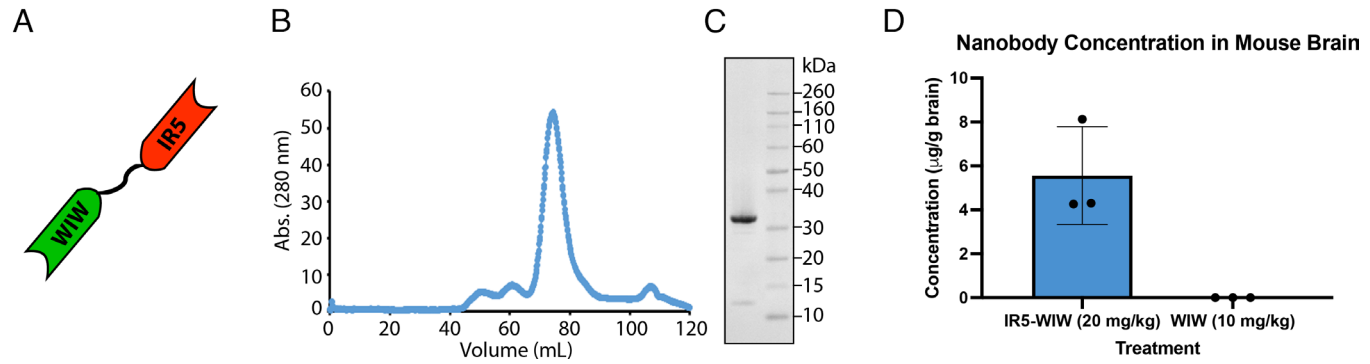

Fig. 5. Designed bispecific nanobody that crosses the BBB. (*A*) The bispecific nanobody constructed by conjoining the WIW nanobody and IR5 Nanobody (46) with a flexible linker of sequence (Gly4Ser)3. (*B*) S75 SEC of the bispecific WIW nanobody showing a prominent species for the collected middle peak fractions. (*C*) SDS-PAGE analysis of prominent bispecific WIW reveals one band with ~30 kDa. (*D*) Concentration of the bispecific nanobody and second-generation WIW nanobody in wild-type mouse brain (n = 3 mice for each nanobody). Nanobodies were quantified using LC–MS/MS.

quality (51); 2) nanobodies possess high structural stability for in vitro and in vivo applications; 3) nanobodies display low immunogenicity risk profile which is beneficial for potential therapeutic applications (52); and 4) nanobodies have a smaller size makes them useful as therapeutics for brain delivery and tissue penetration (28, 53).

We met an important requirement for design specificity by showing the WIW inhibitor segment maintains an epitope-complementary structure after grafting it into a nanobody (Fig. 1*D*). In general, antibodies contain three CDR flexible loops and CDR3 contributes most of the binding specificity for antigenic determinants. We chose to graft WIW into CDR3. After determining the atomic structure of the WIW nanobody inhibitor, we observed that CDR3 adopts a beta-strand secondary structure instead of a flexible loop. It appears preorganized to bind to the tip of the protofilament and prevent fibril elongation (Fig. 1 *E* and *F*).

An important goal of our designed nanobody is to block the seeded spread of pathogenic tau aggregates, so we assayed our panel of designs (WIW, VDW, W3, M4, etc.) using seeds from the brains of a panel of twelve different patients in HEK293 biosensor cells. Experimental evidence suggests that a prion-like seeding mechanism is the main route for propagation and spreading tau pathology in the brain and tau seeding inhibitors may delay or prevent the progress of these maladies (54, 55). We designed two generations of synthetic nanobodies, which differ in nanobody scaffold used. For generation 2, we chose scaffold 2, which exhibits a higher pI (pI = 9.8) than scaffold 1 of generation 1, making generation 2 better candidates for spontaneous cell penetration. The second-generation nanobody inhibitors decrease seeding by AD patient brain extracts in biosensor cells (Fig. 2 and *SI Appendix*, Figs. S2–S4). In addition, the second-generation nanobody inhibitors decrease seeding by purified tau fibrils from AD and PSP patients (Fig. 4 and *SI Appendix*, Fig. S5), demonstrating that aggregation-prone interfaces of both AD and PSP tau are accessible and targeted by our designed nanobody inhibitors.

Although the molecular mechanism that leads to AD is still poorly understood, small oligomers are thought to spread tau pathology and induce neuronal toxicity in the brain (56–58). To further test the efficacy of WIW and SV nanobodies against seeding by tau oligomers, we used IL15-induced tau-K18 oligomers to seed tau in biosensor cells. The WIW and SV designed nanobodies potently inhibit seeding by tau oligomers (Fig. 3 and *SI Appendix*, Fig. S2).

Much atomic-level structural information has supported the view that specific amyloid fibril polymorphs are linked to distinct diseases. Indeed, amyloid protein conformations may define distinct diseases and constitute a basis for classification of amyloid diseases (59). The structures of AD tau and PSP tau fibrils are quite different. In AD, tau adopts two folds: PHFs and SFs, which both consist of an ordered core of pairs of protofilaments comprising residues 306 to 378. Therefore, in AD, VQIVYK is in the ordered core and VQIINK is in the fuzzy coat. In progressive supranuclear palsy (PSP), tau adopted a single protofilament with an ordered core extended from residues 272 to 381 (59). Therefore, in PSP, both VQIVYK and VQIINK are in the ordered core. Our nanobody panels directed toward VQIVYK and VQIINK inhibit tau seeding by purified tau fibrils from ten donors with AD and two donors with PSP, as well as seeding by recombinant tau K18 oligomers, for which the atomic-level structure is not known. This finding suggests that the inhibitor segment seated in the nanobody could be flexible enough to recognize multiple conformations of tau.

In cases of patient AD3, AD8, and the recombinant K18 oligomers (Fig. 2, Fig. 3, and *SI Appendix*, Figs. S4 and S3), we observed some nonspecific inhibition by the noncognate nanobody. It is possible that the nonspecific inhibition comes from some nonspecific binding of tau from the nanobody scaffold. Based on the results of the unbiased docking experiment (*SI Appendix*, Fig. S1 *D* and *E*), we are aware of a few possible configurations of nonspecific binding. However, based on the finding that sequestering monomeric tau with an anti-tau antibody is not sufficient for inhibition (Fig. 2*F*), only nonspecific binding in aggregation-prone regions such as the fibril core or VQIINK could contribute to the nonspecific inhibition in biosensor cells. In future generations of nanobody design, we will select a scaffold with less nonspecific binding and nonspecific inhibition.

Finally, we designed a bispecific nanobody that both serves as a capping inhibitor of tau and targets IGF1R for delivery to the brain via RMT. We administered the bispecific nanobody to three wild-type mice and measured its concentration to be 4.3 to 8.1 μg per g of brain tissue using LC–MS/MS. We administered second-generation WIW to three wild-type mice and did not detect WIW in brain tissue. Our findings are consistent with the hypothesis that fusion of the WIW capping inhibitor with an IGFR1-binding nanobody improved BBB penetration after intravenous administration in mice. Brain delivery is a major limitation of antibody-based therapeutics, so our findings may represent significant progress toward overcoming this limitation.

Because neurofibrillary tangles are formed intracellularly, our nanobodies would need to penetrate the cell membrane or be expressed in the neuronal cytoplasm to halt tau aggregation. We designed our nanobodies with a high pI (above 9.4) because it has been reported that nanobodies with a high pI spontaneously penetrate cells (43). In the future, we plan to investigate whether our

nanobodies penetrate cells spontaneously or require additional modification.

In summary, we used a design approach to produce a panel of nanobody inhibitors that halt prion-like seeding by tau amyloid. By targeting the steric zipper interfaces, we designed a panel of inhibitors able to block cell-to-cell seeding by recombinant tau-oligomers, purified AD brain fibrils, and purified PSP brain fibrils. In addition, we designed a bispecific nanobody that targets IGFR1 and enters the brain via RMT. We provided evidence that the bispecific nanobody improved BBB penetration over the tau capping inhibitor alone after intravenous administration in mice. Taken together, these results demonstrate that we can use structure-based design to engineer antibodies to target tau aggregation and overcome the limitations of traditional antibody production.

Materials and Methods

Tau Protein Expression. Human wild-type tau-K18 (residues 244 to 372) was expressed in a pNG2 vector and purified as previously described (8, 38).

Design, Cloning, Expression, and Purification of Antibody Inhibitors. WIW (scaffold 1), VDW (scaffold 1), W3 (scaffold 1), WIW (scaffold 2), and SV (scaffold 2) antibody genes were synthesized by GenScript and cloned into the pMES4 vector encoded with an N-terminal pelB signal peptide for periplasmic expression and a 6× His-tag at the C-terminal end. W3, M4, R9, and QIINK (scaffold 2) antibody genes were synthesized by Twist Bioscience and cloned into the pMES4 vector using the PstI- BstEII restriction site. The bispecific WIW nanobody was synthesized by GenScript and cloned into the pMES4 vector encoded with an N-terminal pelB signal peptide for periplasmic expression and a 6X His-tag at the C-terminal end. One residue at position 145 was changed from a valine to a glutamic acid to improve protein expression yield. This residue is nonsolvent facing and is outside of the three complementarity determining regions and should not affect protein function. Protein expression and purification were performed according to our previous protocol (38, 44).

Crystallization. The WIW nanobody inhibitor was concentrated to 10 mg/mL and crystallization trials were performed by mixing equal volumes of the protein and reservoir solution. Crystals appeared from cocktails containing 0.15 M ammonium sulfate 0.1 M MES pH5.5 25%w/v PEG 4000 (C10: ProPlex, molecular dimensions) after 7 d at 16 °C. All crystals were cryoprotected with reservoir solution containing 35% (W/V) glycerol and flash-frozen in liquid nitrogen.

X-ray Data Collection and Structure Solution. X-ray data for WIW nanobody inhibitor were collected at beamlines 24-ID-C at the Advanced Photon Source. Data were processed in XDS and XSCALE (60). Molecular replacement was performed with the program PHASER (61), using prion nanobody 484 (Protein Data Bank entry: 6HEQ) as a search model (37). Refinement and structure building was performed in PHENIX (62) and Coot (63).

Docking. To generate figures of the nanobody inhibitor bound to the tau PHF fibril, the crystal structure of the WIW nanobody was aligned to the relevant region of the PHF using Pymol. The beta-strand inhibitor sequence in the nanobody CDR3 region (PDB code: 8FQ7) was aligned to the top fibril layer of the VQIVYK segment of the tau PHF (PDB code: 5O3L) using the Align function of Pymol.

Preparation of tau-k18 Fibrils. Recombinant tau-k18 was diluted to 25 μM and mixed 1× PBS, pH 7.4, 20 mM DTT, 10 mM ThT (thioflavin T), and 5% ionic liquid (HR2-214-15, HamptonResearch). Protein was liquated to 3 replicate wells of a 96-well plate (Thermo Scientific Nunc), and the plate was incubated at 37 °C for 24 h with shaking and a plastic bead to enhance agitation. The amyloid fibril formation was monitored by measuring ThT fluorescence at 440/480 nm excitation and emission wavelengths and examined using negative stain transmission EM.

Preparation and Purification of tau Oligomers. Recombinant tau-K18 at a concentration of 12 μM was incubated in 1× PBS (pH 7.4) with 10 mM DTT and 2% ionic liquid (HR2-214-15, Hampton Research) with shaking for 16 to 18 h at 37 °C in a 96-well plate (Thermo Scientific Nunc) with a plastic bead to enhance agitation. The solution was subsequently centrifuged for 5 min at 14,000 rpm to remove any large aggregates, and the supernatant was concentrated using an ultracentrifugal spin filter with a 10-kDa cutoff (Amicon). Concentrated samples were injected on a HiLoad 16/600 Superdex 75 pg.

Dot blot. Tau-K18 monomer or fibril protein was blotted to a nitrocellulose membrane (Invitrogen). The membrane was blocked in TBST (Tris-buffered saline, pH 7.6, and 0.1% Tween 20) supplemented with 5% milk and incubated with the VDW nanobody (10 μg/mL) in TBST supplemented with 2% milk for 2 h. The membrane was then incubated with HisProbe-HRP (horseradish peroxidase) (Thermo Scientific, Cat No.: 15165), at dilution 1:5,000 in TBST for 1 h.

In the case of human tau-K18 oligomer or monomer fractions (10 μL) purified from SEC were blotted on a nitrocellulose membrane. The membrane was then blocked using 5% milk in TBST for 1 h at RT and followed by three times washing with TBST buffer. The membrane was incubated with monoclonal M204 (1:1,000) in TBST supplemented with 2% milk for 1 h at RT and followed by Goat anti-rabbit HRP (Abcam, ab6721) as a secondary antibody. All membranes were developed using PierceTM ECL Plus substrate (Thermo Scientific, Cat No.: 32132).

Immunogold Electron Microscopy of Nanobody Binding to tau-K18 Fibrils. For immunogold EM, 5 μL of tau-k18 fibrils was applied onto 400-mesh carbon-coated formvar support films mounted on copper grids for 3 min followed by fast blotting. EM grids were blocked with 0.1% gelatin in PBS for 10 min and followed by VDW nanobody at dilution 1:100 into 0.1% gelatin-PBS and incubated with EM grids for 60 min. Then, the EM grids were washed 5× with gelatin-PBS and fast-dried between washes. Grids were applied to the primary antibody (anti-His tag monoclonal antibody (HIS.H8), Invitrogen, Cat # MA1-21315 at 1:1,000 dilution in 1% gelatin-PBS) and incubated for 30 min. Grids followed by incubation at dilution 1:8 with colloidal gold AffiniPure goat anti-Mouse IgG (Jackson Immuno Research Laboratories, Code ID: 115-195-166) for 30 min. The EM grids were washed 5× with water and stained with 4 μL of 2% uranyl acetate for 2 min and followed by washing with an additional 4 μL of 2% uranyl acetate and allowed to dry for 10 min. The grids were imaged using a T12 (FEI) election microscope.

Preparation of Brain Crude tau Seeds. Postmortem tissue for neuropathologically confirmed tauopathy cases from brain regions indicated in *SI Appendix*, Table S3, and figure legends were fresh-frozen and extracted without freeze-thaw. Tissue was cut into a 0.2 to 0.3 g section on a block of dry ice, and then manually homogenized in a 15 mL disposable tube in 1 mL of 50 mM Tris, pH 7.4 with 150 mM NaCl containing 1× HALT protease inhibitor. Samples were then aliquoted to PCR tubes and sonicated in a cuphorn bath for 150 min under 30% power at 4 °C in a recirculating ice water bath, according to reference (64).

Tau Biosensor Cell Maintenance and Seeding. HEK293 cell lines stably expressing tau-K18 P301S-eYFP, referred to as tau biosensor cells were engineered by Marc Diamond's lab at UTSW (65) and used without further characterization or authentication. Cells were maintained in DMEM (Life Technologies, cat. 11965092) supplemented with 10% (vol/vol) FBS (Life Technologies, cat. A3160401), 1% penicillin/streptomycin (Life Technologies, cat. 15140122), and 1% Glutamax (Life Technologies, cat. 35050061) at 37 °C, 5% CO2, in a humidified incubator. Fibrils and patient-derived seeds were incubated at 4 °C for 16 h with nanobody inhibitor to yield a final inhibitor concentration of 10 μM (on the biosensor cells). A noncognate nanobody and an antibody binding to residues 6 to 18 (BioLegend Cat. No. 816601) were used as negative controls. For seeding, inhibitor-treated seeds were sonicated in a cuphorn water bath for 3 min and then mixed with 1 volume of Lipofectamine 2000 (Life Technologies) prepared by diluting 2 μL of Lipofectamine in 18 μL of OptiMEM. After 20 min, 10 μL of seeds was added to 90 μL of tau biosensor cells. After 6 d, the number of seeded aggregates was determined by imaging the entire well of a 96-well plate in triplicate using a Celigo Image Cytometer (Nexcelom) in the YFP channel. Aggregates were counted using ImageJ (66) by subtracting the background fluorescence from unseeded cells and then counting the number of peaks with fluorescence above background using the built-in Particle Analyzer. The number of aggregates was normalized to the confluence of each well, and dose–response plots were generated by calculating the average and SDs from triplicate measurements. For high-quality images, cells were photographed on a ZEISS Axio Observer D1 fluorescence microscope using the YFP fluorescence channel.

Fibril Extraction of AD and PSP Brain Tissues. The extraction of fibrils from human tissue was performed according to previous protocol (45).

Negative-Stain Transmission Electron Microscopy. EM samples were prepared by applying 5 μL of Tau-K18 oligomers or AD and PSP filaments to glow-discharged grid CF150-Cu 150 mesh carbon films mounted on copper grids (Electron Microscopy Sciences) and incubating on the grid for 3 min. The samples were then blotted off and the grids were stained with 12 μL of 2% uranyl acetate for 2 min. The grids were blotted off and allowed to dry for 10 min. Grid was imaged using a T12 (FEI) electron microscope.

Immnogold Electron Microscopy of Extracted tau Fibrils. Nanogold particle binding was performed as described (67). Four microliters of sarkosyl insoluble tau fibril extracted from AD patients was used with primary antibody Tau46 (BioLegend cat#806604, 1:100 dilution in 1% gelatin-PBS) and secondary goat anti-mouse antibody (Jackson ImmunoResearch Laboratories Inc cat# 115-195-146, 1:8 dilution in 1% gelatin-PBS). TEM images were acquired with a FEI Tecnai T12 transmission electron microscope at 120kV.

Cell Viability Assay. Neuro-2a cells (ATCC catalog # CCL-131) were cultured in MEM media (Life Technologies catalog # 11095-080) with 10% FBS (Life Technologies catalog # 10437010) and 1% penicillin–streptomycin (Life Technologies catalog # 15140122) in a 5% CO_2 incubator at 37 °C. N2a cells were plated onto clear 96-well plates (Costar catalog # 3596) at 5,000 cells/well in 90 μL culture media. After 24 h, the nanobody was added at various concentrations. After incubation for an additional 24 h, 20 μL thiazolyl blue tetrazolium bromide MTT dye (Sigma; 5 mg/mL stock in DPBS) was added to each well and then incubated for 3.5 h at 37 °C. Removal from the incubator and replacement of well media with 100 μL of 100% DMSO halted the assay. Absorbance was measured at 570 nm using a SpectraMax M5 reader. A background reading at 700 nm was subtracted from the 570 nm reading. Well readings were normalized to vehicle-alone–treated cells (designated as 100% viable) and cells treated with 100% DMSO (designated as 0% viable).

Animal Experiments. All animal experiments were approved by the UCLA Animal Research Committee and performed under the oversight of the Division of Laboratory Animal Medicine. C57BL/6J mice (Jackson Laboratories: JAX:000664) were housed on a 12-h light/dark schedule.

Sample Preparation for LC–MS/MS Analysis. Mice were injected intravenously with the bispecific nanobody (IR5-WIW) at a concentration of 20 mg/kg (n = 3) or the second-generation WIW nanobody at a concentration of 10 mg/kg (n = 3) and killed by perfusion 30 min postinjection. Brains were collected by standard dissection and immediately frozen. For each brain, 100 mg was dissected and homogenized in 1 mL of 1× SDS buffer (2% SDS, pH 6.8) with a Fisherbrand 850 Homogenizer for 15 s. Next, each 1 mL of homogenate was concentrated using a Labconco CentriVap Benchtop Vacuum Concentrator to 500 μL. Each brain homogenate (90 μL) was mixed with 30 μL of loading dye including β-mercaptoethanol and urea. Next, 40 μL of the brain homogenate/loading dye mixture was run in three wells of a NuPAGE™ 4 to 12%, Bis–Tris, 1.0 mm, 10-well gel. Coomassie blue–stained bands were then excised for LC–MS/MS sample preparation. For brain samples with IR5-WIW, the gel was cut in the range of 20 to 30 kDa. For brain samples with WIW, the gel was cut in the range of 10 to 15 kDa. Additional details about the tryptic digestion, tandem mass spectrometry, and quantification by parallel reaction monitoring are provided in *SI Appendix, Supplementary Materials and Methods*. Proteomic datasets submitted to the ProteomeXchange Consortium through the MassIVE repository are identified as PXD043069.

Data, Materials, and Software Availability. 1) Plasmid for bacterial expression of nanobodies, 2) X-ray crystallography structure, 3) coordinate for WIW nanbody inhibitor, 4) proteomic datasets data have been deposited in 1) Addgene, 2) Protein Data Bank, 3) Protein Data Bank, 4) ProteomeXchange Consortium through the MassIVE repository with ID number 1) 205574 (68), 10.2210/pdb8fq7/pdb 2) 8FQ7 (69), 3) PXD043069 (70). All other study data are included in the article and/or *SI Appendix*.

ACKNOWLEDGMENTS. This work is based upon research conducted at the Northeastern Collaborative Access Team (NECAT) beamlines, which are funded by the National Institute of General Medical Sciences from the NIH (P30 GM124165). The Pilatus 6M detector on 24-ID-C beam line is funded by an NIH-ORIP HEI grant (S10 RR029205). This research used resources of the Advanced Photon Source, a US Department of Energy (DOE) Office of Science User Facility operated for the DOE Office of Science by Argonne National Laboratory under Contract No. DE-AC02-06CH11357. We thank the staff of the NECAT beamlines for their expert support. We also acknowledge 1R01AG070895 (D.S.E.), R01 AG048120 (D.S.E.), and RF1AG056507 (C.G.G.) from the National Institute on Aging, 1F32 NS095661 from the National Institute of Neurological Disorders and Stroke (P.M.S.), R35GM145286 from the National Institute of General Medical Sciences (J.A.L.), A2016588F from the BrightFocus Foundation (P.M.S.), and HHMI for support. We thank the NIH NeuroBioBank for providing tissues under request #1306. H.P. is supported by the UCLA–Caltech Medical Scientist Training Program (GM08042) and the UCLA Chemistry–Biology Interface Training Grant (US Public Health Service National Research Service Award 5T32GM008496). E.O. acknowledges support by the National Institute of General Medical Sciences of the NIH under Award Number T32GM145388. C.L. acknowledges support from the Ruth L. Kirschstein National Research Service Award program (GM007185).

Author affiliations: [a]Department of Chemistry and Biochemistry, UCLA, Los Angeles, CA 90095; [b]Department of Biological Chemistry, UCLA, Los Angeles, CA 90095; [c]HHMI, UCLA, Los Angeles, CA 90095; [d]UCLA-Department of Energy Institute, Molecular Biology Institute, UCLA, Los Angeles, CA 90095; [e]Molecular Instrumentation Center, UCLA, Los Angeles, CA 90095; [f]VIB-Vrije Universiteit Brussel Center for Structural Biology, VIB and Vrije Universiteit Brussel, Brussels B-1050, Belgium; [g]Department of Pathology and Laboratory Medicine, David Geffen School of Medicine, UCLA, Los Angeles, CA 90095; [h]Department of Neurology, David Geffen School of Medicine, UCLA, Los Angeles, CA 90095; [i]Department of Neurology, University of California San Francisco Weill Institute for Neurosciences, University of California, San Francisco, CA 94143; [j]Department of Pathology, University of California, San Francisco, CA 94143; and [k]Department of Molecular Biology and Biochemistry, University of California, Irvine, CA 92697

Author contributions: R.A., H.P., and D.S.E. designed research; R.A., H.P., M.R.S., P.M.S., E.J.O., Y.C., K.A.M., J.Z., C.L., M.B., D.R.B., D.C., B.A.N., K.H., X.C., E.P., J.S., C.G.G., R.R.O.L., J.A.L., and D.S.E. performed research; C.K.W., A.L.N., H.V.V., S.S., L.T.G., and W.W.S. contributed new reagents/analytic tools; R.A., H.P., M.R.S., P.M.S., E.J.O., Y.C., K.A.M., J.Z., C.L., M.B., D.R.B., D.C., B.A.N., E.P., J.S., C.G.G., R.R.O.L., J.A.L., and D.S.E. analyzed data; and R.A., H.P., and D.S.E. wrote the paper.

1. G. K. Wilcock, M. M. Esiri, Plaques, tangles and dementia. A quantitative study. *J. Neurol. Sci.* **56**, 343–356 (1982).
2. D. J. Selkoe, The molecular pathology of Alzheimer's disease. *Neuron* **6**, 487–498 (1991).
3. J. A. Hardy, G. A. Higgins, Alzheimer's disease: The amyloid cascade hypothesis. *Science* **256**, 184–185 (1992).
4. J. I. Ayers, B. I. Giasson, D. R. Borchelt, Prion-like spreading in tauopathies. *Biol. Psychiatry* **83**, 337–346 (2018).
5. M. Goedert, D. S. Eisenberg, R. A. Crowther, Propagation of tau aggregates and neurodegeneration. *Annu. Rev. Neurosci.* **40**, 189–210 (2017).
6. D. J. Selkoe, J. Hardy, The amyloid hypothesis of Alzheimer's disease at 25 years. *EMBO Mol. Med.* **8**, 595–608 (2016).
7. D. S. Eisenberg, M. R. Sawaya, Neurodegeneration: Taming tangled tau. *Nature* **547**, 170–171 (2017).
8. P. M. Seidler *et al.*, Structure-based inhibitors of tau aggregation. *Nat. Chem.* **10**, 170–176 (2018).
9. S. A. Sievers *et al.*, Structure-based design of non-natural amino-acid inhibitors of amyloid fibril formation. *Nature* **475**, 96–100 (2011).
10. J. Zheng *et al.*, Macrocyclic beta-sheet peptides that inhibit the aggregation of a tau-protein-derived hexapeptide. *J. Am. Chem. Soc.* **133**, 3144–3157 (2011).
11. M. R. Sawaya *et al.*, Atomic structures of amyloid cross-beta spines reveal varied steric zippers. *Nature* **447**, 453–457 (2007).
12. P. M. Seidler *et al.*, Structure-based inhibitors halt prion-like seeding by Alzheimer's disease-and tauopathy-derived brain tissue samples. *J. Biol. Chem.* **294**, 16451–16464 (2019).
13. M. von Bergen *et al.*, Assembly of tau protein into Alzheimer paired helical filaments depends on a local sequence motif ((306)VQIVYK(311)) forming beta structure. *Proc. Natl. Acad. Sci. U.S.A.* **97**, 5129–5134 (2000).
14. A. W. P. Fitzpatrick *et al.*, Cryo-EM structures of tau filaments from Alzheimer's disease. *Nature* **547**, 185–190 (2017).
15. T. Arakhamia *et al.*, Posttranslational modifications mediate the structural diversity of tauopathy strains. *Cell* **180**, 633–644.e12 (2020).
16. B. Falcon *et al.*, Novel tau filament fold in chronic traumatic encephalopathy encloses hydrophobic molecules. *Nature* **568**, 420–423 (2019).
17. B. Falcon *et al.*, Structures of filaments from Pick's disease reveal a novel tau protein fold. *Nature* **561**, 137–140 (2018).
18. W. Zhang *et al.*, Novel tau filament fold in corticobasal degeneration. *Nature* **580**, 283–287 (2020).
19. E. M. Sigurdsson, Tau Immunotherapies for Alzheimer's Disease and related tauopathies: Progress and potential pitfalls. *J. Alzheimers Dis.* **66**, 855–856 (2018).

20. R. Steinbrook, The accelerated approval of aducanumab for treatment of patients with Alzheimer disease. *JAMA Intern. Med.* **181**, 1281 (2021).
21. M. Bi, A. Ittner, Y. D. Ke, J. Gotz, L. M. Ittner, Tau-targeted immunization impedes progression of neurofibrillary histopathology in aged P301L tau transgenic mice. *PLoS One* **6**, e26860 (2011).
22. A. A. Asuni, A. Boutajangout, D. Quartermain, E. M. Sigurdsson, Immunotherapy targeting pathological tau conformers in a tangle mouse model reduces brain pathology with associated functional improvements. *J. Neurosci.* **27**, 9115–9129 (2007).
23. A. Boutajangout, D. Quartermain, E. M. Sigurdsson, Immunotherapy targeting pathological tau prevents cognitive decline in a new tangle mouse model. *J. Neurosci.* **30**, 16559–16566 (2010).
24. M. Roberts *et al.*, Pre-clinical characterisation of E2814, a high-affinity antibody targeting the microtubule-binding repeat domain of tau for passive immunotherapy in Alzheimer's disease. *Acta Neuropathol. Commun.* **8**, 13 (2020).
25. X. Chai *et al.*, Passive immunization with anti-Tau antibodies in two transgenic models: Reduction of Tau pathology and delay of disease progression. *J. Biol. Chem.* **286**, 34457–34467 (2011).
26. A. Mullard, Failure of first anti-tau antibody in Alzheimer disease highlights risks of history repeating. *Nat. Rev. Drug. Discov.* **20**, 3–5 (2021).
27. P. Sormanni, F. A. Aprile, M. Vendruscolo, Rational design of antibodies targeting specific epitopes within intrinsically disordered proteins. *Proc. Natl. Acad. Sci. U.S.A.* **112**, 9902–9907 (2015).
28. S. Muyldermans, Nanobodies: Natural single-domain antibodies. *Annu. Rev. Biochem.* **82**, 775–797 (2013).
29. C. Hamers-Casterman *et al.*, Naturally occurring antibodies devoid of light chains. *Nature* **363**, 446–448 (1993).
30. C. Morrison, Nanobody approval gives domain antibodies a boost. *Nat. Rev. Drug. Discov.* **18**, 485–487 (2019).
31. G. C. Terstappen, A. H. Meyer, R. D. Bell, W. Zhang, Strategies for delivering therapeutics across the blood-brain barrier. *Nat. Rev. Drug. Discov.* **20**, 362–383 (2021).
32. W. Zhang *et al.*, Differential expression of receptors mediating receptor-mediated transcytosis (RMT) in brain microvessels, brain parenchyma and peripheral tissues of the mouse and the human. *Fluids Barriers CNS* **17**, 47 (2020).
33. W. Alata *et al.*, Targeting insulin-like growth factor-1 receptor (IGF1R) for brain delivery of biologics. *FASEB J.* **36**, e22208 (2022).
34. D. B. Stanimirovic, J. K. Sandhu, W. J. Costain, Emerging technologies for delivery of biotherapeutics and gene therapy across the blood-brain barrier. *BioDrugs* **32**, 547–559 (2018).
35. M. Ribecco-Lutkiewicz *et al.*, A novel human induced pluripotent stem cell blood-brain barrier model: Applicability to study antibody-triggered receptor-mediated transcytosis. *Sci. Rep.* **8**, 1873 (2018).
36. J. M. Perchiacca, A. R. Ladiwala, M. Bhattacharya, P. M. Tessier, Structure-based design of conformation- and sequence-specific antibodies against amyloid beta. *Proc. Natl. Acad. Sci. U.S.A.* **109**, 84–89 (2012).
37. R. Abskharon *et al.*, Structural evidence for the critical role of the prion protein hydrophobic region in forming an infectious prion. *PLoS Pathog.* **15**, e1008139 (2019).
38. R. Abskharon *et al.*, Crystal structure of a conformational antibody that binds tau oligomers and inhibits pathological seeding by extracts from donors with Alzheimer's disease. *J. Biol. Chem.* **295**, 10662–10676 (2020).
39. I. T. Desta, K. A. Porter, B. Xia, D. Kozakov, S. Vajda, Performance and its limits in rigid body protein-protein docking. *Structure* **28**, 1071–1081.e3 (2020).
40. D. C. Rodriguez Camargo *et al.*, Proliferation of tau 304–380 fragment aggregates through autocatalytic secondary nucleation. *ACS Chem. Neurosci.* **12**, 4406–4415 (2021).
41. C. A. Lasagna-Reeves *et al.*, Tau oligomers impair memory and induce synaptic and mitochondrial dysfunction in wild-type mice. *Mol. Neurodegener.* **6**, 39 (2011).
42. C. A. Lasagna-Reeves *et al.*, Alzheimer brain-derived tau oligomers propagate pathology from endogenous tau. *Sci. Rep.* **2**, 700 (2012).
43. T. Li *et al.*, Cell-penetrating anti-GFAP VHH and corresponding fluorescent fusion protein VHH-GFP spontaneously cross the blood-brain barrier and specifically recognize astrocytes: Application to brain imaging. *FASEB J.* **26**, 3969–3979 (2012).
44. R. N. Abskharon *et al.*, Probing the N-terminal beta-sheet conversion in the crystal structure of the human prion protein bound to a nanobody. *J. Am. Chem. Soc.* **136**, 937–944 (2014).
45. M. Schmidt *et al.*, Cryo-EM structure of a transthyretin-derived amyloid fibril from a patient with hereditary ATTR amyloidosis. *Nat. Commun.* **10**, 5008 (2019).
46. J. Sheff *et al.*, Defining the epitope of a blood–brain barrier crossing single domain antibody specific for the type 1 insulin-like growth factor receptor. *Sci. Rep.* **11**, 4284 (2021).
47. D. Wessel, U. I. Flugge, A method for the quantitative recovery of protein in dilute solution in the presence of detergents and lipids. *Anal. Biochem.* **138**, 141–143 (1984).
48. C. K. Hua *et al.*, Computationally-driven identification of antibody epitopes. *Elife* **6**, e29023 (2017).
49. R. J. Pantazes, C. D. Maranas, OptCDR: A general computational method for the design of antibody complementarity determining regions for targeted epitope binding. *Protein Eng. Des. Sel.* **23**, 849–858 (2010).
50. K. E. Tiller, P. M. Tessier, Advances in antibody design. *Annu. Rev. Biomed. Eng.* **17**, 191–216 (2015).
51. A. de Marco, Recombinant expression of nanobodies and nanobody-derived immunoreagents. *Protein Expr. Purif.* **172**, 105645 (2020).
52. C. Ackaert *et al.*, Immunogenicity risk profile of nanobodies. *Front. Immunol.* **12**, 632687 (2021).
53. D. Wrapp *et al.*, Structural basis for potent neutralization of betacoronaviruses by single-domain camelid antibodies. *Cell* **181**, 1004–1015.e15 (2020).
54. A. Mudher *et al.*, What is the evidence that tau pathology spreads through prion-like propagation? *Acta Neuropathol. Commun.* **5**, 99 (2017).
55. F. Clavaguera *et al.*, Transmission and spreading of tauopathy in transgenic mouse brain. *Nat. Cell Biol.* **11**, 909–913 (2009).
56. M. R. Brier *et al.*, Tau and abeta imaging, CSF measures, and cognition in Alzheimer's disease. *Sci. Transl. Med.* **8**, 338ra366 (2016).
57. S. J. Jackson *et al.*, Short fibrils constitute the major species of seed-competent tau in the brains of mice transgenic for human P301S tau. *J. Neurosci.* **36**, 762–772 (2016).
58. C. Cardenas-Aguayo Mdel, L. Gomez-Virgilio, S. DeRosa, M. A. Meraz-Rios, The role of tau oligomers in the onset of Alzheimer's disease neuropathology. *ACS Chem. Neurosci.* **5**, 1178–1191 (2014).
59. Y. Shi *et al.*, Structure-based classification of tauopathies. *Nature* **598**, 359–363 (2021).
60. W. Kabsch, Xds. *Acta Crystallogr. D Biol. Crystallogr.* **66**, 125–132 (2010).
61. A. J. McCoy *et al.*, Phaser crystallographic software. *J. Appl. Crystallogr.* **40**, 658–674 (2007).
62. P. D. Adams *et al.*, PHENIX: A comprehensive Python-based system for macromolecular structure solution. *Acta Crystallogr. D Biol. Crystallogr.* **66**, 213–221 (2010).
63. P. Emsley, B. Lohkamp, W. G. Scott, K. Cowtan, Features and development of Coot. *Acta Crystallogr. D Biol. Crystallogr.* **66**, 486–501 (2010).
64. S. K. Kaufman, K. Del Tredici, T. L. Thomas, H. Braak, M. I. Diamond, Tau seeding activity begins in the transentorhinal/entorhinal regions and anticipates phospho-tau pathology in Alzheimer's disease and PART. *Acta Neuropathol.* **136**, 57–67 (2018).
65. D. W. Sanders *et al.*, Distinct tau prion strains propagate in cells and mice and define different tauopathies. *Neuron* **82**, 1271–1288 (2014).
66. C. A. Schneider, W. S. Rasband, K. W. Eliceiri, NIH Image to ImageJ: 25 years of image analysis. *Nat. Methods* **9**, 671–675 (2012).
67. K. A. Murray *et al.*, De novo designed protein inhibitors of amyloid aggregation and seeding. *Proc. Natl. Acad. Sci. U.S.A.* **119**, e2206240119 (2022).
68. D. Eisenberg, Structure-based design of nanobodies that inhibit seeding of Alzheimer's patient-extracted tau fibrils: WIW_Scaffold2. Addgene. https://www.addgene.org/205574/. Deposited 7 July 2023.
69. R. Abskharon, M. R. Sawaya, D. C. Cascio, D. S. Eisenberg, Nanobody with WIW inserted in CDR3 loop to inhibit growth of Alzheimer's Tau fibrils. Protein Data Bank. https://www.rcsb.org/structure/8FQ7. Deposited 5 January 2023.
70. D. S. Eisenberg, J. A. Loo, R. R. Ogorzalek Loo, PRM and DDA data for IR5 WIW and WIW nanobodies. MassIVE. https://massive.ucsd.edu/ProteoSAFe/QueryPXD?id=PXD043069. Deposited 17 June 2023.